IEEE Access
Multidisciplinary ⋮ Rapid Review ⋮ Open Access Journal

Received 23 July 2023, accepted 11 August 2023, date of publication 21 August 2023, date of current version 30 August 2023.

Digital Object Identifier 10.1109/ACCESS.2023.3306952

RESEARCH ARTICLE

Study of Magneto-Thermal Problems in Low-Speed High-Torque Direct Drive PMSM Based on Demagnetization Detection and Loss Optimization of Permanent Magnets

PENG ZHOU[1], YANLIANG XU[1], AND FENG XIN[2]
[1]School of Electrical Engineering, Shandong University, Jinan 250061, China
[2]Shandong Institute for Product Quality Inspection, Jinan 250102, China

Corresponding author: Yanliang Xu (xuyanliang@sdu.edu.cn)

This work was supported in part by the Science and Technology Major Project of Shandong Province under Grant 2022CXGC020404, and in part by the National Science Foundation of China under Grant U22A2021.

ABSTRACT Low-speed high-torque direct drive permanent magnet synchronous motor (LHDD-PMSM) can suffer from a typical magneto-thermal coupling problem during long periods of continuous load operation, resulting in temperature rise and leading to reversible demagnetization of the permanent magnets (PMs), thus affecting the motor's operational performance. In this paper, we experimentally verify the existence of the magneto-thermal problem and investigate methods to reduce the magneto-thermal coupling problem. The paper first researches the on-line detection method of reversible demagnetization. As reversible demagnetization in motors is difficult to identify, we propose a method by measuring the transient PM back EMF of the motor to detect the magnetic properties of PMs in the field. And furtherly, an on-line tester is developed to detect the reversible demagnetization of the LHDD-PMSM. Secondly, this paper analyses the main sources of PM losses and proposes an electromagnetic optimized model combining mixed structure magnetic slot wedge and rotor magnetic insulation slot, so that the eddy current loss of PMs can be greatly weakened. Finally, a bi-directional coupled magneto-thermal simulation model is established with the comparison to a temperature rise experiments, and the model can be used to illustrate the improvement of the magneto-thermal problem of LHDD-PMSM by the loss reduction method proposed in the paper.

INDEX TERMS No-load back EMF, permanent magnet eddy current loss, reversible demagnetization, slot wedge, tooth harmonics.

I. INTRODUCTION

Low-speed high-torque direct drive permanent magnet synchronous motor (LHDD-PMSM) has the advantages of simple structure, easy maintenance, small size, high efficiency, high power factor and easy control ability. Because the direct drive motor does not require the reducer, it is widely used in various engineering and equipment manufacturing fields. The magnetic stability of permanent magnets (PMs) in LHDD-PMSM are the basis for achieving its expected performance in operation. Therefore, at the beginning of motor design, the designer needs to fully consider the possibility of demagnetization [1], [2]. The causes of demagnetization include chemical corrosion, physical destruction, armature reverse magnetic field [3], [4], [5] and temperature rise [6], [7], [8]. The first two demagnetization reasons are generally irreversible and often caused by the harsh environment. However, the latter two are reversible or not depend on the working point of the PM. If the working point of PMs is located above the knee point of its demagnetization curve, the change of magnetic properties is reversible, but if it is located below the knee point, the demagnetization will be irreversible.

The associate editor coordinating the review of this manuscript and approving it for publication was Feifei Bu.

Temperature rise demagnetization is one of the most common types of demagnetization phenomena in the operation of PMSMs. Modern high-performance PMSMs generally use Nd-Fe-B as the PM material, but the magnetic properties of Nd-Fe-B are very susceptible to temperature. In PM motors, in order to prevent demagnetization of PMs caused by excessive losses, it is necessary to make a careful analysis of the sources of losses in rotor and PMs at initial design. For LHDD-PMSMs driven by inverters, there are two main sources of eddy current (EDC) losses in the PMs. One is from the harmonic magnetic field generated by the high order harmonic current, and the other is from the tooth harmonic magnetic field generated by the stator slotting. The latter is closely related to the structural characteristics of the LHDD-PMSM and the motor production process. On the one hand, in order to increase the torque density, the LHDD-PMSM is designed with larger electrical loads, so flat wire prefabricated windings and parallel slots are commonly used in the design, which increases the slot fill factor and the number of conductors per slot. On the other hand, in order to facilitate the insertion of flat wire pre-formed windings, open slots are commonly used for stator slots in LHDD-PMSM. Due to the significant differences in magnetic permeability between stator teeth and slots, the magnetic field experiences significant fluctuations at the slot opening in the motor air gap. As a result, the tooth harmonics in the LHDD-PMSM often exhibit low orders and high amplitudes, compared to other types of motor. In high-speed motors, the stator slots of the motor are smaller and the orders of current harmonics are higher. Therefore, the percentage of permanent magnet EDC losses generated by current harmonics are relatively large [9]. However, the slot type and the winding structure still have a large impact on the EDC losses of the PMs [10], [11]. Hence, in the LHDD-PMSM, the amplitude of tooth harmonics increases substantially, leading to more significant losses, thereby becoming the primary cause of PM heating and demagnetization [12].

The EDC losses in PMs have various adverse effects on the operation of PMSMs. Larger EDC losses not only result in rotor overheating, impacting the magnetic properties of the magnets, but they can also leads to changes in the stress distribution in the rotor, which has an impact on the mechanical strength of the rotor [13], [14].

Furthermore, the continuous heat generation from PMs due to sustained EDC losses can trigger a positive feedback loop of temperature rise within the motor and result in reversible demagnetization of the magnets. Such phenomena are occasionally observed in long-term loaded permanent magnet motors. This paper aims to conduct research on this type of reversible demagnetization issue, exploring detection techniques, and optimization solutions.

This paper presents an analysis case of an electric motor applied in a cross-regional water transfer pumping station. The LHDD-PMSM installed in the water pump operates continuously for several months. Due to inadequate heat dissipation conditions for the PMs, when the ambient temperature rises, the original thermal balance of the motor system is disrupted, leading to a decrease in heat dissipation efficiency. As the PMs are sensitive to temperature, their magnetic performance only experiences a slight decline at the beginning. However, under constant external load on the motor, the reduction in magnetic load needs to be balanced by an increase in electrical load, causing a passive increase in armature current and generating additional heat. This further elevates the temperature of the PMs and enters a positive feedback process of temperature rise. This cycle continues until a new thermal balance is reached. Since the motor still operates within a reasonable operating range, the changes in magnetic performance of the PMs are generally reversible. When the motor stops and cools down, the performance of motor can return to the original state. However, during the process of reversible demagnetization of the PMs, the armature current of LHDD-PMSM gradually and continuously increases, leading to increased losses and decreased system efficiency, resulting in a continuous decline in operational economy. Specially, for large-scale LHDD-PMSM units, although reversible demagnetization does not cause direct damage to the motor in the short term, addressing the positive feedback issue will not only yield significant economic benefits, but also be benefit for extending the motor's operational lifespan.

The study of this paper will be conducted from two perspectives: magnetic demagnetization detection and PM loss suppression. Firstly, this paper aims to verify the existence of temperature rise positive feedback phenomenon in LHDD-PMSM during actual operation, which can be achieved through real-time monitoring of the demagnetization status of the PMs in the motor. Clearly, traditional offline methods for detecting the magnetic performance of PMs are improper in this application [13], because the demagnetization in LHDD-PMSM have a strong correlation with operating conditions and ambient temperature. Meanwhile, there are some online detection methods for demagnetization based on signal processing, but these algorithms are rather complex, and the accuracy of demagnetization judgment is very dependent on the accuracy of the detected signal [15], [16]. Therefore, this paper will firstly propose a simple real-time online method for detecting the magnetic performance of the permanent magnets. Secondly, in order to suppress the occurrence of temperature rise positive feedback during motor operation, it is essential to address the heat generation at the source, which is related to the PM losses. This study will investigate methods to reduce PM losses within the constraints of the existing manufacturing process and structure of LHDD-PMSM.

Based on the series of issues presented above, this paper is organized as follow:

In Section II, a magnetic performance online detection method for PMSMs based on the waveform equivalence theory of back electromotive force is proposed. This method

is utilized to experimentally detect the temperature rise reversible demagnetization phenomenon in LHDD-PMSM.

In Section III, from the perspective of suppressing PM losses and temperature rise, the sources of EDC losses of PMs in LHDD-PMSM under different operating conditions are analyzed.

In Section IV, the optimization of air-gap tooth harmonics is considered as the focal point for reducing PM losses and heat generation. To reduce tooth harmonics' amplitude, a hybrid structure slot wedge is introduced. Additionally, a rotor slot insulation is introduced to lower the harmonic distortion in the air-gap magnetic field. The hybrid slot wedge and the rotor slot insulation are combined to propose an improved model capable of significantly reducing the tooth slot effects and permanent magnet eddy current losses.

In Section V, a bi-directional magneto-thermal coupled model is established to compare the temperature rise between the original model and the optimized model, and the temperature rise experiment of LHDD-PMSM is used as a reference. The comparison results aim to validate the efficacy of the proposed PM loss suppression method in reducing motor temperature rise, mitigating the positive feedback process, and enhancing the operational economy.

II. REVERSIBLE DEMAGNETIZATION DETECTION OF PERMANENT MAGNETS

The prototype of this paper is shown in Fig. 1, and its rated parameters are as follows: rated power 1800kW, line voltage 6300V, rated frequency 50Hz, pole number 48, and rated speed 125rpm.

FIGURE 1. Physical picture of the researched LHDD-PMSM.

As mentioned earlier, the motor requires a long period of continuous load operation. Table 1 shows the motor operation data changes of stator current I, active power P and reactive power Q during 7 days of continuous operation.

According to the operation data, the reasons can be assumed as follows: After the motor is started up, the heat dissipation effect of PM is inadequate, causing its temperature rise continuously, leading to demagnetization of the PMs. According to motor design theory, on the premise of fixed size, the electromagnetic torque of the motor can be summarized as (2) from the basic motor size formula (1).

$$C_A = \frac{D^2 l_{ef}}{P'/n} = \frac{60D^2 l_{ef}}{2\pi T'} = \frac{6.1}{\alpha'_p K_{Nm} K_{dp} A B_\delta} \tag{1}$$

$$T = K \cdot Ka \cdot Kv \cdot IaB\delta \tag{2}$$

TABLE 1. Continuous load experiment test data.

Time	I (A)	P (kW)	Q (k·Var)
0h	120	1231.578	285.735
24h	123	1257.821	296.294
48h	127	1298.621	318.724
72h	129	1314.613	321.581
96h	132	1319.981	310.719
120h	134	1377.652	329.636
144h	133	1332.197	321.373
168h	133	1337.553	317.085

where K represents the proportionality constant, K_a represents the winding coefficient, K_v represents the volume coefficient. For manufactured motors, K_a and K_v are fixed values. I_a is the armature current, representing the electrical load, and B_δ is amplitude of the air gap magnetic density, representing the magnetic load.

The above equation indicates that the output torque of the motor is determined by both the magnetic load and the electrical load. With the reduction of the magnetic load, the stator current passively increases to balance the load, which further aggravates the overall temperature of the motor, further reduces the magnetic performance of the PMs, and makes the above process enter continuous positive feedback until the temperature of the motor rises to a balance where the heat generation equal to heat dissipation. Therefore, the stator current, active power and reactive power will migrate to a higher value.

According to the assumption, if demagnetization is caused by temperature rise, the magnetic properties of the permanent magnet will recover as the motor is powered off and cooled. That is, when starting up again, if the load remains unchanged, the stator current will continue to remain at 120A. Obviously, the transient load of the pump station during the water transfer process is uncertain, so in practice, it is difficult to use the magnitude of the stator current as an indicator to determine whether the motor has undergone reversible demagnetization.

In order to verify the assumption, the most effective way is to test the magnetic properties of the PMs directly. Without disassembling the motor and removing PMs, the magnetic properties of the PMs can be characterized by the no-load back EMF E_0 of the PMSM. The relationship between E_0 and permanent magnet magnetic linkage can be described by (3):

$$E_0 = p \cdot \omega_0 \cdot \psi_0 \tag{3}$$

where p represents the number of pole pairs; ω_0 represents the mechanical angular velocity; Ψ_0 represents the permanent magnetic flux chain passing through the winding.

The traditional method for measuring no-load back EMF of PMSM is motor drag test, but it is not suitable for the reversible demagnetization detection in this paper. The reasons are as follow:

(1) The drag test needs to build a separate test-bed, and the test motor needs to be disassembled from its installation environment. The cost of test is too high.

(2) The reversible demagnetization of PMs is closely related to the dynamic heating of the motor, so the test of E_0 must be on-site and real-time.

Aiming at the existing shortcomings, this paper proposes an online detection method (ODM) and an online detection tester (ODT) for the test of no-load back EMF of PMSM.

A. OPERATION PRINCIPAL OF ODM

For a manufactured PMSM, both the pole pairs and the permanent magnet flux linkage under a certain temperature are fixed values. Therefore, the E_0 of the PMSM is proportional to the rotational speed of the rotor as (4).

$$\frac{E_1}{E_2} = \frac{\omega_1}{\omega 2} = \frac{n_1}{n_2} \tag{4}$$

This equation shows that if the no-load back EMF of PMSM at a certain speed n_1 (or angular velocity ω_1)is known, its back EMF at other speed n_2 (or ω_2)can be calculated according to the speed ratio.

When a PMSM rotates at constant speed, the waveform of E_0 is approximately a sine wave with constant amplitude and period. However, when it rotates at a variable speed, E_0 will be no longer a standard sine wave. At any moment, the amplitude and frequency of the waveform are variable. Fig.2 shows the measured waveform of E_0 when the rotor decelerates freely under resistive torque after the motor is powered off. It can be seen that the waveform looks like a sine wave, but at any moment, the amplitude and frequency synchronously decline as the rotational speed decreases.

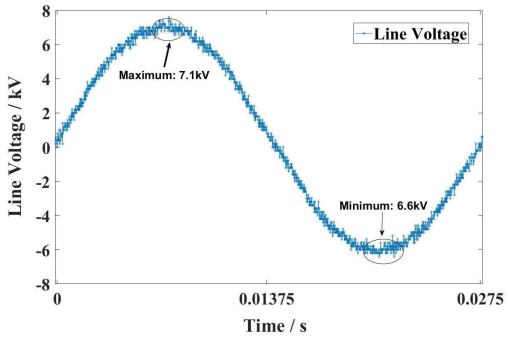

FIGURE 2. Waveform of E_0 when the rotor decelerates freely.

Although the waveform is non-sinusoidal, there is a specific constraint relationship between the E_0 and flux linkage Ψ, which represents the total flux passing through the winding. When the motor is under no-load condition, Ψ represents the permanent magnet flux. The voltage equation of the PMSM during no-load operation is shown in (5).

$$E_0 = u = \frac{d\psi}{dt} \tag{5}$$

When the motor is powered off, the rotor decelerates freely. During this period, taking winding A as an example, the relationship between its E_0 and Ψ is shown in Fig.3.

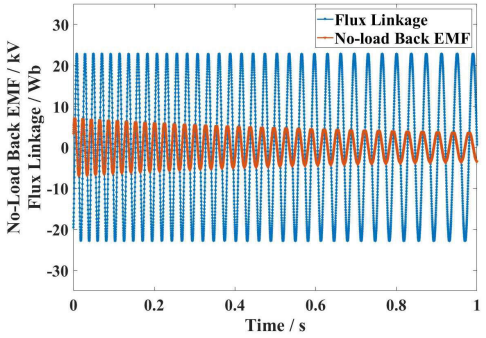

FIGURE 3. No-load back EMF vs. flux linkage.

Since the waveform is not sinusoidal, the electrical cycle can be defined as the period that the rotor rotating over a pair of magnetic poles. Calculate an integral for $|E_0|$ within an electrical cycle, as shown in (6).

$$\begin{aligned}\int_0^T |E_0(t)| \cdot dt &= \int_0^{t1} |E_0(t)| \cdot dt + \int_{t1}^{T} |E_0(t)| \cdot dt \\ &= \int_0^{t1} \left|\frac{d\psi(t)}{dt}\right| \cdot dt + \int_{t1}^{t2} \left|\frac{d\psi(t)}{dt}\right| \cdot dt \\ &= |\psi(t)|_{t=0} + 2\,|\psi(t)|_{t=t1} + |\psi(t)|_{t=t2} \\ &= 4\psi_{PM}\end{aligned} \tag{6}$$

where T represents the total time of an electrical cycle, the waveform between $0 \sim t_1$ is a positive half-cycle wave, and $t_1 \sim t_2$ is a negative one.

It can be seen from the above formula that in an electrical cycle, regardless of whether the waveform is sinusoidal or not, the integral interval can be divided into two parts based on the positive and negative values of E_0. The integral result for each part is twice that of the amplitude of the permanent magnet flux linkage passing through the phase winding. Therefore, the integral of $|E_0|$ within an electrical cycle is a constant, which is determined only by the flux linkage generated by the PMs.

Divide both sides of (6) by the electrical cycle T to obtain the average value of E_0, as shown in (7). It can be seen that if T remains constant, the average value of the waveform is a constant.

$$\frac{1}{T}\int_0^T |E_0(t)| \cdot dt = \frac{4\psi_{PM}}{T} \tag{7}$$

From the above derivation, it can be seen that although the amplitude and frequency of the waveform vary arbitrarily with the rotational speed, the average value of the waveform within an electrical cycle is deterministic. And it can be further seen from (6) that the waveform equivalence method holds true whether the rotor is in an accelerated or decelerated state after power off, since the integral of $|E_0|$ over the integer number of electrical cycles is only related to the maximum

value of Ψ_{PM}. Therefore, the waveform of E_0 within integer electrical cycle can be equivalent to a standard sine wave with the same average value and period.

B. DEVELOPMENT AND TEST OF ODT

Based on the above principle, a prototype ODT is designed. The on-line measurements proposed in this paper are performed based on the equivalence of the waveforms after the motor has been powered off. Since the above test can be accomplished by processing the signal for only one electrical cycle, the measurement process is very fast. For a 50 Hz based motor, the total time for measurement and signal processing is less than 50ms. In order to realize the ODM algorithm under test, the ODT can send power-off signal to the motor controller or receive power-off signal from it, thus capturing dynamic waveform after the motor has been powered off. After the capturing of waveform, the no-load back EMF of the motor at the rated speed is calculated through (4) to (7). When the measurement is complete, the ODT could send signals to the motor controller, which controls the motor to resume operation.

The tester is designed based on the stm32F4 and AD7606 chips as shown in Fig. 4, and an experimental platform for checking the measuring accuracy of ODT is built as shown in Fig. 5 to compare the results measured by the drag test with ODM. The tested motor is a 4-pole PMSM with a rated rotational speed of 1500 rpm. The experiment was divided into three groups based on different initial speeds. The results are presented in Table 2. From the data, it can be seen that the testing results of ODM is precise enough to be applied to the reversible demagnetization detection of LHDD-PMSM.

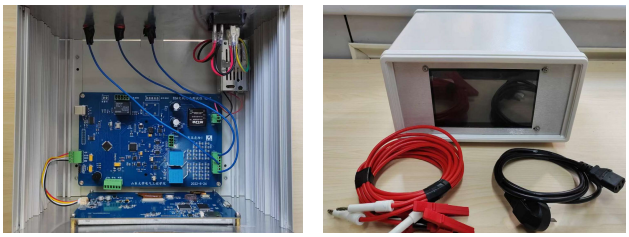

FIGURE 4. The prototype of ODT.

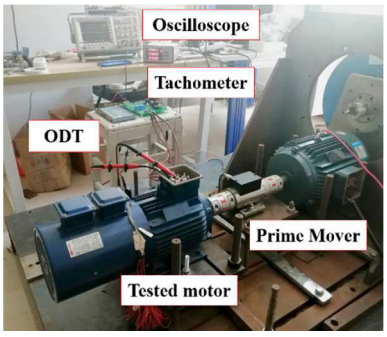

FIGURE 5. Test platform of ODT.

TABLE 2. Comparison of experimental data.

	Test 1	Test 2	Test 3
Initial Speed (rpm)	1250	1000	750
On-line Test Value (V)	270.731	270.466	270.478
Drag Test Value (V)		270.831	
Equivalent Error	0.37‰	1.35‰	1.30‰

C. REVERSIBLE DEMAGNETIZATION TEST OF LHDD-PMSM

Establish a test environment to measure the no-load back EMF of LHDD-PMSM by using ODT, as shown in Fig. 6. Since the voltage level (10kV) of LHDD-PMSM is high, the motor needs to be connected to a voltage transformer and the ODT measures the voltage signal after voltage reduction.

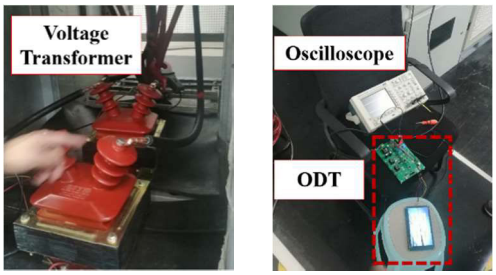

FIGURE 6. The establishment of test environment.

In order to detect the reversible demagnetization of LHDD-PMSM through the test of no-load back EMF, three sets of comparative experiments are designed, which are described as follows:

a. E_1 is measured by the test during the first run of the motor;

b. E_2 is measured by the test after 7 days of continuous load operation of the motor;

c. E_3 is measured by the test after 30 minutes of shutdown and cooling down of the motor.

The RMS values of no-load back EMF of LHDD-PMSM obtained from three tests are shown in Table 3. Comparing E_2 with E_1, it can be seen that the no-load back EMF of the motor decreased from 6341.39V to 6056V after 7 days of continuous operation under load, with a decrease of 4.5%. From Eq. (1), it can be known that the magnetic flux provided by the PMs reduce to a same degree, indicating that the PMs are demagnetized during continuous operation. Compared with E_3 and E_1, the difference between them is greatly reduced, indicating that the magnetic performance of the PMs gradually recovers with the cooling of the motor, and the demagnetization is reversible due to the temperature rise.

TABLE 3. Comparison of three groups of test results.

	E_1	E_2	E_3
Value (V)	6341.39	6056	6320.21
D-value (V)	/	283.39	20.82
Percentage	/	4.5%	0.23%

As mentioned earlier, with the decline in magnetic performance, the armature current and active power of motor increase continuously. Due to the constant power output, all of the increased active power is converted into heat, resulting in a continuous reduction in the efficiency. According to the comparison of the data from the experiments, the source of the demagnetization can be determined as temperature rise. In order to control the temperature rise of PMs, it is necessary to analyze the sources of losses in LHDD-PMSM.

III. ANALYSIS OF THE LOSS SOURCES OF PMS

Nd-Fe-B is widely used as the PMs in PMSM. It is electrically conductive and its conductivity is about 625000 Siemens/m. Therefore, when an alternating magnetic field passes through the PM, the changing magnetic field will produce eddy current, which will lead to loss. The EDC losses of the PMs can be determined by (8):

$$\begin{aligned} P &= \int_V \sigma \vec{E}^2 dV = \int_V \frac{\vec{J}^2}{\sigma} dV \\ &= \frac{1}{T}\int_0^T \int_0^h \int_0^{lpm} \int_{-t_2}^{t_2} \frac{J^2(x,t)}{\sigma} dxdydzdt \\ &= \sum_{k=1}^{n} \frac{\sigma h l_{pm} \tau^3 B_{mk}^2 \omega_{ek}^2}{8} \left(\frac{\delta}{3\tau} \frac{\sinh(\frac{\delta}{\tau}) - \sin(\frac{\delta}{\tau})}{\cosh(\frac{\delta}{\tau}) - \cos(\frac{\delta}{\tau})} \right) \end{aligned} \tag{8}$$

where E represents the EDC electric field strength, J represents the EDC density, σ represents the electrical conductivity of PM, V represents the volume of the PM, n represents the number of spatial harmonics, B_n represents the magnetic density amplitude of the nth spatial harmonic, ω_n represents the angular frequency of the nth EDC harmonic induced inside the PM, δ_n represents the penetration depth of the nth spatial harmonic in the PM, and τ_n represents the polar distance of the nth spatial harmonic.

Equation (8) can be further reorganized as (9), where $k_n(\delta, \tau)$ represents the EDC coefficient of the corresponding nth spatial harmonic, which is a function of the penetration depth of that harmonic in the PM and its own polar distance.

$$P = \sum_{k=1}^{n} k_n(\delta, \tau) B_{mk}^2 f_{ek}^2 V \tag{9}$$

From this equation it can be seen that the alternating magnetic field passing through the PMs is the source of EDC losses. the magnitude of which is proportional to the square of the frequency and amplitude of the magnetic field.

Ideally, the air gap magnetic fields generated by the stator and the rotor rotate at a synchronous speed, thus inducing no EDC in PMs. However, in practice, there are many harmonic components in the air gap which have spatial relative motion with the rotor. The specific analysis is as follows.

When the PMSM runs without load, the air gap magnetic field is only the permanent magnet magnetic field. Taking the single layer PM rotor as an example and assuming that the motor has no slots, the air gap magnetic field is a flat top wave, which contains the fundamental wave and odd spatial harmonic component. They all rotate at synchronous speed and remain relatively static with the PMs. However, due to the slotting in the stator, the actual motor will introduces abundant tooth harmonic in the air gap. The order of tooth harmonics can be determined by (10):

$$\nu = \frac{Q}{p} \pm 1 = 2mq \pm 1 \tag{10}$$

where Q is the number of slots, p is the number of pole pairs, m is the number of phases, and q is the number of slots per phase per pole. Both the fundamental wave and the spatial magnetic field harmonics in the air gap are affected by the slot and then generate the tooth harmonics. Tooth harmonics do not rotate synchronously with the PMs, thus generating EDC loss and heat on PMs. Fig.7 compares the waveform and its Fourier transform of the air-gap magnetic field before and after slotting. It is clear that the new component in the air-gap is due to slotting.

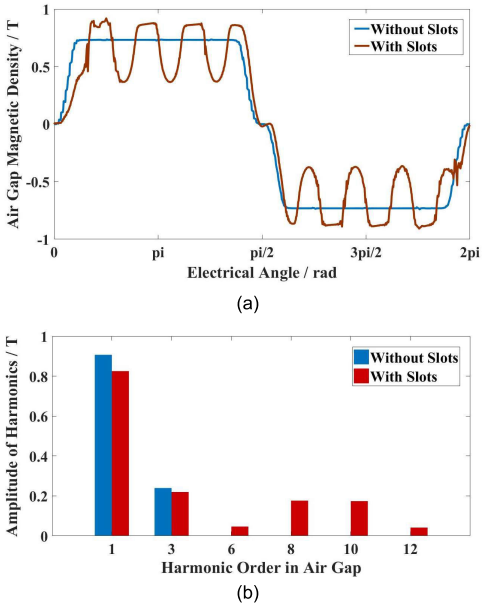

FIGURE 7. Comparison of the waveforms and theirs Fourier transform.

When the PMSM is under load, the air gap magnetic field is established by the combination of the PM and the armature. In order to simplify the analysis, it is assumed that the magnetic circuit saturation is not taken into account, so that the permanent and armature magnetic fields can be analyzed separately.

The permanent magnetic field has been discussed above. In the previous analysis, tooth harmonics are the only source of PMs losses. For armature magnetic field, taking double-layer short-distance distributed windings as an example, when the armature current does not contain harmonics, the air gap armature magnetic field contains the synchronous fundamental component and the asynchronous harmonic magnetic field of $6K \pm 1$ times. Similar to the permanent magnetic field, the former will also be affected by slots to generate

tooth harmonics, which will cause loss of the PMs. The latter can be greatly weakened by the short-pitch and distribution of the windings, so it can be ignored in the analysis of EDC loss of PMs. It can be seen from Fig.8 that the amplitude of the tooth harmonics increases obviously due to the overlap of the tooth harmonics in the armature magnetic field and permanent magnet magnetic field. As stated in (9), the density of the EDC loss is proportional to the square of the harmonic amplitude, so the EDC loss of the PMs under load will be further increased compared to no-load condition.

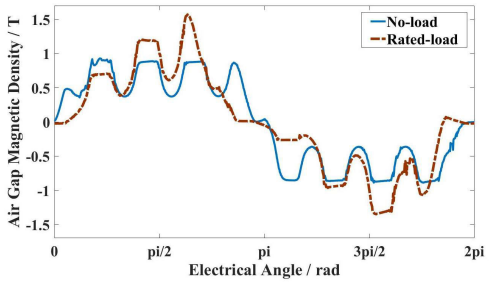

FIGURE 8. Comparison of magnetic field waveforms under no-load and rated-load condition.

In practice, adjust-speed PMSMs are mostly powered by inverters, so the spatial harmonics caused by the current harmonics which are introduced by the inverters are also an important source of EDC losses in PMs. In high-speed motors, due to the high rated frequency, if the harmonic distortion rate of the output current of inverter is high, the EDC losses will greatly increase. However, in low-speed direct drive motors, the rated frequency is around power frequency, so the harmonic frequency is relatively low. Therefore, the EDC losses of the PMs caused by current harmonics is far less than that of high-speed motors. Meanwhile, the optimal design of converters is not the purpose of this paper, so the EDC losses caused by current harmonics will not be discussed further.

In summary, stator slotting and poor quality of air gap magnetic fields are the main reasons for EDC losses of PMs in LHDD-PMSM. Therefore, in order to reduce the temperature rise of PMs in LHDD-PMSM, it is necessary to make further research on tooth harmonic reduction and air gap magnetic field optimization in the paper.

IV. STUDY ON LOSS REDUCTION OF PM IN LHDD-PMSM

A. MAGNETIC SLOT WEDGE

Tooth harmonics are caused by the abrupt changes of magnetic permeability in the air gap. Therefore, the reduction of tooth harmonics can be achieved by minimizing the magnetic permeability variations between the teeth and slots.

As mentioned earlier, the no-load air gap magnetic field waveform of the motor is close to the flat top wave when the slot is not considered, that is, in addition to the fundamental wave, it also contains odd harmonics such as 3rd and 5th orders. For the prototype in the paper, when the open slot is introduced, the tooth harmonics generated by the fundamental and spatial harmonic magnetic field can be calculated by (10), as shown in Table 4.

TABLE 4. Main tooth harmonic order and amplitude.

	Order/Amplitude	Order/ Amplitude
1st	8 / 0.177T	10 / 0.175T
3rd	6 / 0.048T	12 / 0.041T
5th	4 / 0.019T	14 / 0.010T
7th	2 / 0.005T	16 / 0.003T

It can be seen from the table that the amplitude of the 5th spatial harmonics and above are small, so the amplitude of the generated tooth harmonics are smaller. Therefore, the 6th, 8th, 10th, and 12th tooth harmonic generated by the fundamental wave and the 3rd spatial harmonic are the main research objects in this paper.

A 1/24 2-demension finite element model (FEM) of LHDD-PMSM is established. The main design parameters is shown in Table 5, and the model is shown in Fig. 9.

TABLE 5. Design data of LHDD-PMSM.

Parameters	Value
Outer/inner Diameter of Stator (mm)	2600/2150
Air Gap Width (mm)	4
Axial Length (mm)	520
Slot Type	Open Slot
Width/height of Slot (mm)	18/185
Br/Hc of Permanent Magnet (T/ (kA/m))	1.155/820
Number of PM Blocks	10
Dimensions of Single PM (mm)	115*48*21

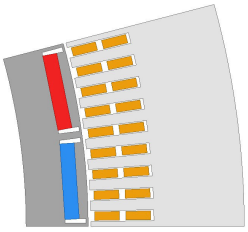

FIGURE 9. The FEM of LHDD-PMSM.

The effect of tooth harmonics can be weakened by a rational design of the stator tooth shoe or by introducing a magnetic slot wedge. The design of the LHDD-PMSM, however, is limited by the winding installation process and therefore cannot be designed flexibly for the type of slot and teeth. Therefore, this sub-section will focus on the effect of magnetic slot wedges on the weakening of tooth harmonics.

Magnetic slot wedges can be formed by adding magnetic conductive materials to traditional non-magnetic slot wedge materials (such as wood, resin, glass fiber, etc.). The introduction of magnetic slot wedge can reduce the variation of the air gap permeability and then reduce the tooth harmonic.

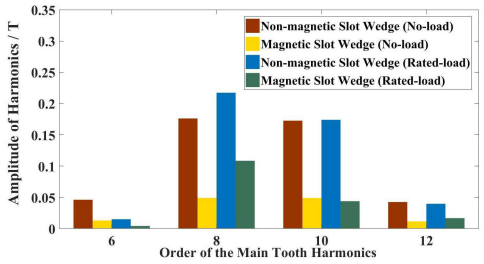

FIGURE 10. Comparison of tooth harmonics before and after the intro-duction of magnetic slot wedges.

Fig.10 compares the amplitude of the main tooth harmonics of the LHDD-PMSM under no-load and rated load conditions when using a magnetic slot wedge or not (wedge thickness h=4mm and relative permeability $\mu = 6$).

It can be seen that after the introduction of the magnetic slot wedge, the major tooth harmonics in the LHDD-PMSM air gap are weakened both at no-load and rated load.

Changes in the μ and h can affect the amplitude of tooth harmonics, which in turn affects the EDC losses of the PMs. Fig.11 shows the trend of EDC losses of PMs under no-load and rated-load as the changes of μ and h.

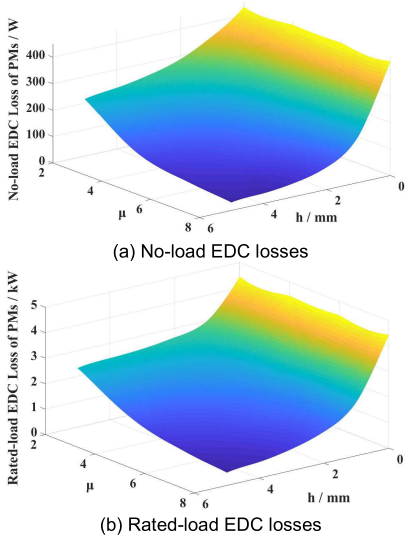

FIGURE 11. Trend of EDC loss of PMs.

As shown above, the no-load EDC loss and load EDC loss of PMs decrease marginally as the magnetic μ and h increase. When magnetic slot wedges are not used, the EDC loss of the PMs under rated load is 3476.7W, while when slot wedges are used with $\mu = 6$ and h=4mm, the EDC loss is 829.2W, and the loss decreases by 76.15%.

Due to the need to reserve as much space as possible in the slot for wire embedding, if the structural strength meets the requirements, the thickness of the slot wedge should be as thin as possible. At the same time, controlling the volume of the slot wedge is also beneficial for reducing its own loss and heat generation. Therefore, to further reduce tooth harmonics and EDC losses of PMs, it is necessary to increase the permeability.

In recent years, soft magnetic composite materials (SMC) have been increasingly used in electrical machines [17], [18], [19]. Compared to traditional slot wedge materials, SMC has higher relative permeability, and has the advantages of magneto-thermal isotropy and easy molding, which are suitable for making slot wedge. However, it also has shortcomings such as lower saturation magnetic density and higher iron loss at low alternating frequency of magnetic field when comparing with Si-steel sheets, making it not suitable be used in the main magnetic circuit of a motor. However, if SMC is applied in slot wedges, the above weak points will not be apparent. The permeability of SMC is superior to that of traditional magnetic slot wedges and weaker than that of laminated silicon steel, enabling it to not only neutralize the permeability changes in air gap, but also limit the flux leakage between stator teeth. When SMC is used as the slot wedge, it can maintain a small volume to reduce losses, and the slot wedge is installed on the side of the air gap, which is also beneficial for its heat dissipation.

The grade of SMC material used in the simulation is Somaloy 700HR 5P, and its B-H and B-P characteristic curves are shown in Fig. 12(a) and Fig. 12(b)

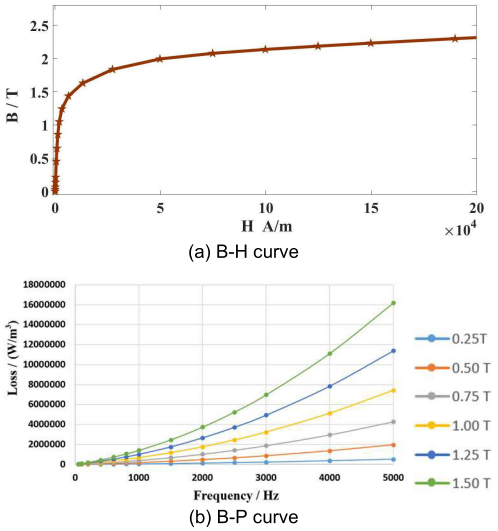

FIGURE 12. B-H and B-P curves of Somaloy 700HR 5P.

Using SMC slot wedge, the variation of the EDC losses of the PMs against the wedge thickness under no-load and rated-load conditions is obtained through simulation, as shown in Fig. 13(a) and Fig. 13(b).

The variation trend of no-load EDC loss of PMs is analyzed firstly. Fig. 14 graphically illustrates the changes in the main magnetic circuit of the motor before and after the introduction of SMC slot wedge when the motor is no-load.

Due to the higher permeability of SMC, the no-load EDC losses are rapidly eliminated as the thickness of the slot wedge increases. As shown in Table 6, comparing the original model with the model using 3mm SMC slot wedge, it can be

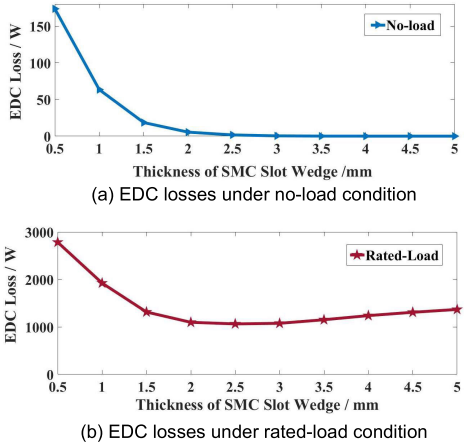

(a) EDC losses under no-load condition

(b) EDC losses under rated-load condition

FIGURE 13. Variation trend of rated-load EDC loss.

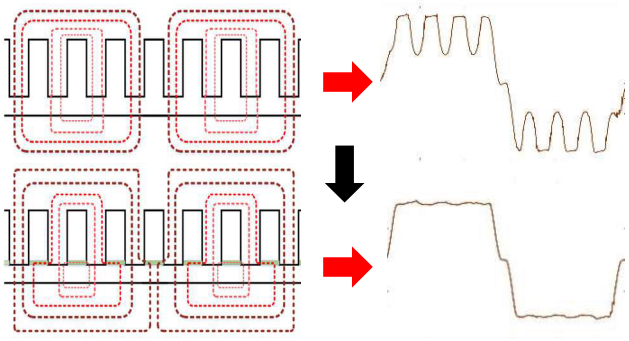

FIGURE 14. Effect of SMC slot wedge on magnetic circuit.

TABLE 6. Variation of harmonic in air gap magnetic density.

Order	Without slot wedge	SMC slot wedge	Variation
1st	0.825T	0.894T	↑
3rd	0.219T	0.239T	↑
6th	0.048T	0.001T	↓
8th	0.177T	0.008T	↓
10th	0.175T	0.007T	↓
12th	0.041T	0.001T	↓

seen from their Fourier decomposition of the no-load air gap magnetic field that the SMC slot wedge almost completely eliminates the 6th, 8th, 10th, and 12th tooth harmonics. As the amplitudes of the tooth harmonics are weakened, the corresponding air gap fundamental and third harmonic magnetic field are enhanced.

As can be seen from Fig.13(b), compared to the trend of no-load EDC loss, when using SMC slot wedges, the load EDC loss first decreases and then slowly increases with the increase of thickness. The turning point of the loss curve is between 2mm and 3mm. Clearly, the variation trend of load EDC loss is not consistent with that at no-load, so further discussion is needed.

To simplify the analysis, it is assumed that the saturation in the main magnetic circuit of the motor is ignored. Therefore, based on the idea of superposition theorem, the load air gap magnetic field can be decomposed into permanent magnetic field generated by PMs and armature magnetic field generated by windings. As mentioned earlier, SMC has a significant effect on reducing tooth harmonics in the air gap permanent magnet magnetic field. Therefore, the effect of SMC slot wedges on armature magnetic field will be researched separately.

Replace the PMs in the model with air and apply a rated current to the stator winding. By parameterizing the thickness of the slot wedge h, the waveform of the air gap magnetic density under a pair of poles at different h is obtained, as shown in Fig. 15.

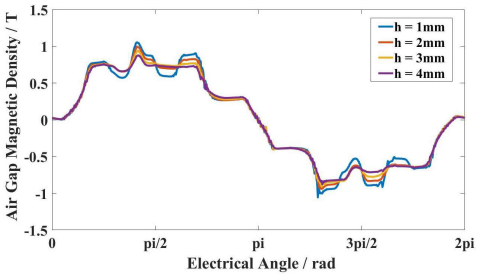

FIGURE 15. Variation of armature magnetic field with h.

As can be seen from Fig.15, as h increases, the waveform of the air gap armature magnetic field gradually changes from a sine wave to a flat top wave. This change can be better understood by combining Fig.16 and Table 7.

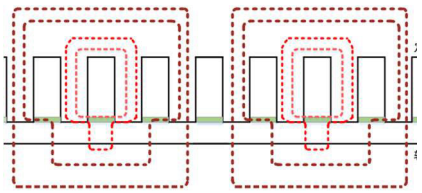

FIGURE 16. Simplified magnetic circuit model.

TABLE 7. Variation of each order harmonics.

Order	h=1mm	h=2mm	h=3mm	h=4mm
1st	0.824T	0.829T	0.815T	0.796T
3rd	0.035T	0.028T	0.032T	0.043T
6th	0.036T	0.059T	0.073T	0.079T
8th	0.175T	0.126T	0.102T	0.087T
10th	0.063T	0.031T	0.018T	0.013T
12th	0.005T	0.009T	0.012T	0.012T

After introducing the SMC slot wedge, the main magnetic circuit of the armature magnetic field is shown in Fig.16. As can be seen, due to the good permeability of SMC, the

flux lines of the stator side do not directly pass through the teeth and enter the air gap, but instead flow into the slot wedge and then into the teeth with lower saturation, or enter the air gap from SMC, resulting in the air gap magnetic field that originally had a sinusoidal distribution being averaged. At the same time, a large number of flux lines close along the slot wedge at the edge of the armature magnetic field, resulting in magnetic leakage. After the redistribution of the magnetic field, the fundamental wave decreases due to the average effect and edge leakage, but the amplitudes of odd harmonics like 3rd and above increase instead. The amplitude changes of them in the air gap magnetic field are shown in Table 7.

The table compares the variation trends of the amplitude of fundamental wave, third harmonic wave, and the main tooth harmonic wave of the air gap magnetic field during the change of h from 1mm to 4mm. According to the previous analysis, it can be clearly seen that due to the averaging effect and magnetic leakage, the fundamental wave first rises and then decreases. However, the third harmonic first decreases and then increases significantly. Under this influence, the 6th and 12th tooth harmonics also increased significantly.

When using SMC slot wedges, the variation trend of the 3rd harmonic wave is consistent with the variation of the load EDC loss of the PMs, as shown in Fig. 17.

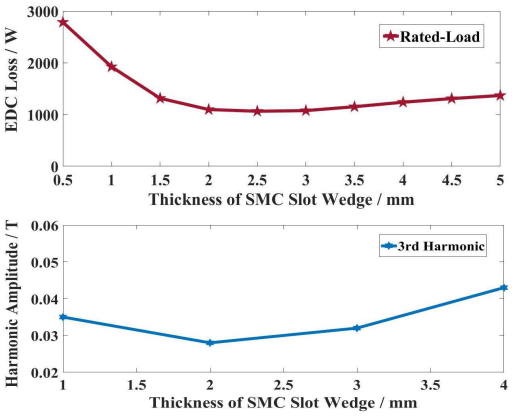

FIGURE 17. Variation trends of loss and third harmonic.

Combining the independent analysis of the permanent and the armature magnetic field, the amplitude variation of the fundamental wave in the overlapping air gap magnetic field is unknown, but the amplitude of odd spatial harmonics such as the 3rd increases significantly with the increase of h.

The above analysis supposes that saturation does not occur in the magnetic circuit. In fact, various regions of the motor, especially the slot wedge, are always in a state of high saturation due to the flow of flux lines.

Fig. 18 shows the B-H curve of the SMC material. It can be seen that the relative permeability of the material decreases significantly at saturation, indicating that the ability of SMC to suppress tooth harmonics is limited at this time. Therefore, as h increases, the amplitude of odd spatial harmonics

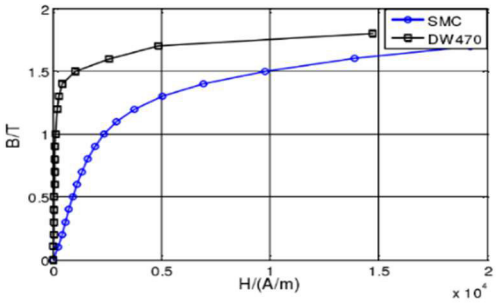

FIGURE 18. Comparison of B-H curves of SMC and DW470.

gradually increases. At the same time, with the saturation of the slot wedge, the ability of the slot wedge to suppress tooth harmonics decreases. These two factors will jointly lead to a further increase in the amplitude of the tooth harmonic waves, leading to higher EDC losses of PMs.

The analysis process is shown in Fig. 19 in detail.

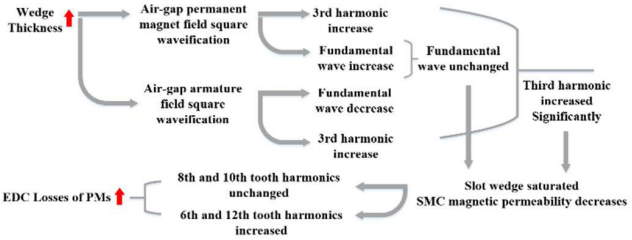

FIGURE 19. Analysis of the causes of loss trends.

From the above analysis, it can be seen that although SMC material has better isotropic magnetic permeability, the problems caused by the magnetic field averaging effect and the saturation nonlinearity of SMC material make it unsuitable for making magnetic slot wedges individually. Preventing the flux lines from closing along the teeth is the key to solving the above problems.

Using the high permeability magnetic material as slot wedge can completely suppress the tooth harmonic in the air gap when the magnetic circuit is not saturated, thereby eliminating the EDC loss of the PMs during no-load operation of the LHDD-PMSM. Using the material with low permeability as slot wedge can block lateral magnetic leakage between teeth, effectively suppressing the EDC losses when the magnetic density in the air gap and the load of the motor is high. Therefore, the characteristics of the two types of slot wedges can be integrated to minimize EDC losses of PMs under all operating conditions of the motor, from no-load to rated-load. Combine the above two schemes and introduce two types of mixed structure slot wedges as shown in Fig.20.

Type 1 places SMC material in the middle of the wedge, with low permeability magnetic materials on both sides. The idea is to add a ''virtual tooth'' between two teeth, thereby increasing the order of tooth harmonics and reducing the amplitude. The arrangement of type 2 is opposite to that of

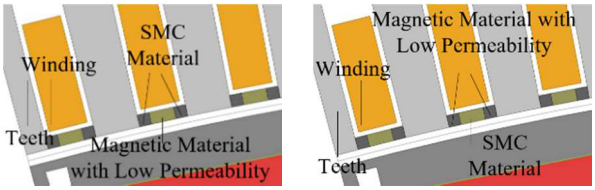

FIGURE 20. Two types of mixed structure slot wedge.

type 1. The idea is to add a tooth shoes whose magnetic permeability is similar to that of the original stator tooth, and combine the low permeability magnetic slot wedge in the middle to further weaken the amplitude of tooth harmonics. Compared to the scheme using only SMC, both schemes utilize low permeability magnetic materials to solve the problem of magnetic leakage between teeth.

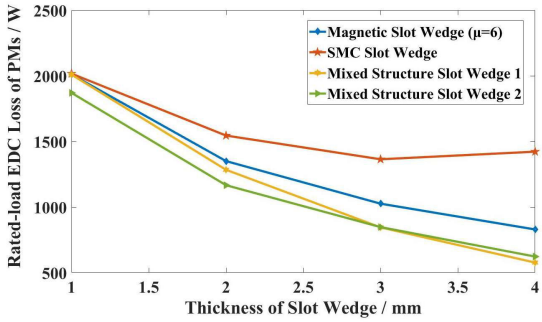

FIGURE 21. Comparison of EDC Loss reduction for different wedges.

As shown in Fig.21, a parametric simulation of the thickness of a mixed structure slot wedge is performed. It can be seen that the EDC loss of the PMs under rated load monotonously decreases as the thickness h increases. Moreover, under the same h, the reduction ability of the two mixed structures on PM losses is significantly better than that of a single material slot wedge.

When the slot wedge thickness is 4mm, the losses of PMs and electromagnetic performance comparison between the original model and the two mixed slot wedge models is shown in Table 8. It can be seen that the optimized EDC losses of the PMs are significantly reduced. When the SMC is placed on both sides, the no-load EDC loss of the PMs is smaller, but the load EDC loss is slightly larger. Further. In addition, the no-load back EMF, rated torque, and torque ripple of the motor are also optimized.

B. ROTOR MAGNETIC INSULATION SLOT

As previously known, the increase of 3rd odd order spatial harmonics is one of the main reasons for the rise in EDC losses of PMs under load. Although the spatial harmonics rotate synchronously with the rotor and do not have the relative motion with the PMs, the tooth harmonics generated by them are still important sources of PM losses.

TABLE 8. Comparison of original and mixed slot wedge model.

	Original	Mixed 1	Mixed 2
No-load EDC Loss (W)	438	51.64	3.33
Rated-load EDC Loss (W)	3476.7	576.8	622.6
Phase Back EMF (V)	4154.51	4363.59	4463.08
Rated Torque (kN.m)	136.36	140.27	143.21
Torque Ripple (kN.m)	14.87	6.43	5.06

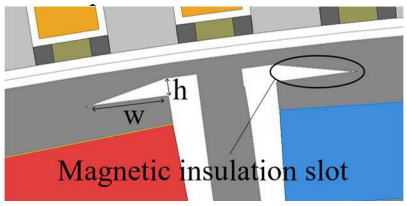

FIGURE 22. Rotor magnetic insulation slot.

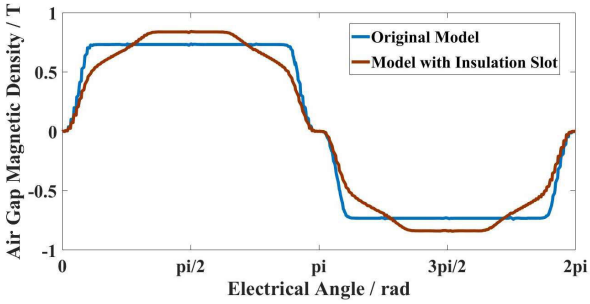

FIGURE 23. Waveform Comparison of air gap magnetic field before and after the introduction of rotor magnetic insulation slot.

A rotor magnetic insulation slot as shown in Fig.22 is introduced, in order to reduce spatial harmonics in the air gap magnetic field and increase the proportion of fundamental wave, so that the permanent magnetic field could converge towards the centerline of magnetic pole. As shown in Fig.23, when the influence of slotting is ignored, by comparing the no-load air gap magnetic field waveform with and without rotor magnetic insulation slots, it can be seen that after adding magnetic insulation slots, the waveform distribution becomes more sinusoidal.

Parametric simulation was conducted on the width w and height h of the rotor magnetic insulation slot, and the variation trend of the no-load EDC loss and the load EDC loss of the PMs with the two factors was shown in Fig.24. With the increase of the w and h, the no-load EDC loss first decreases, then slightly increases, and the EDC loss under rated load decreases monotonically. When the size of the magnetic insulation slot is taken as h=*4*mm and w=*45*mm, the EDC loss of the PMs under rated load drop from *3443.4*W to *2587.3*W.

C. INTEGRATED OPTIMIZED MODEL

Combining the above-mentioned mixed structure slot wedge and rotor magnetic insulation slot, two optimized models are obtained. In the models, the two mixed structures proposed above are selected for the slot wedge, with the wedge

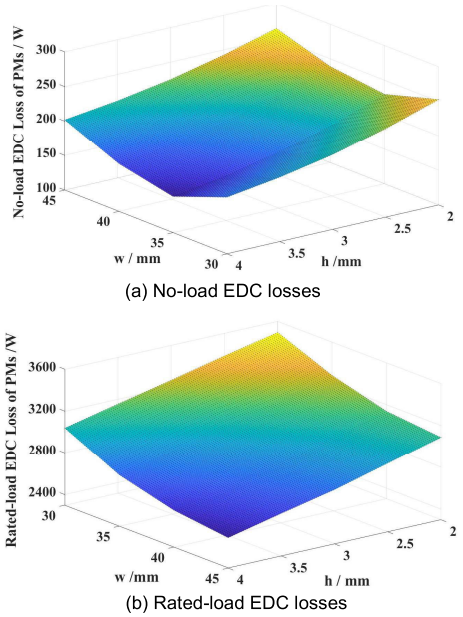

FIGURE 24. Trend of EDC losses of PMs.

thickness of *4*mm, the magnetic insulation slot width of *45*mm, and the thickness of 4mm.

The electromagnetic performance of the original model and the two optimized models of LHDD-PMSM is compared under rated current, as shown in Table 9. It can be seen that with the addition of rotor magnetic insulation slots, the second optimized model has more advantages in loss reduction and electromagnetic performance improvement. Compared to the original model, the no-load EDC loss of PMs in model 2 is almost eliminated, while the EDC loss at rated load is also reduced by 90.7%. In addition, the other electromagnetic properties of the motor are also well improved compared to the original one.

TABLE 9. Comparison of original and optimized model.

	Original	Optimized 1	Optimized 2
Wedge Type	/	Mixed 1	Mixed 2
Rotor Insulation slot	No	Yes	Yes
No Load EDC Loss of PMs (W)	438.1	19.3	0.7
Rated Load EDC Loss of PMs (W)	3476.7	339.6	323.5
No load Back EMF (V)	4154.5	4467.9	4560.8
Rated Torque (kN)	136.4	140.1	143.1
Torque Ripple (kN)	14.9	4.8	4.2

V. TEMPERATURE RISE REDUCTION OF PERMANENT MAGNETS

The EDC loss of PMs is one of the heat sources of motor heating. In fact, after introducing ferromagnetic materials, the slot wedge is inevitably affected by the air gap magnetic field, resulting in iron loss and heat generation. However, compared to interior PMs with poorer heat dissipation conditions, the heat of the slot wedge can be directly carried away by convection in the air gap. This is equivalent to ''replacing'' heat from areas that are not easy to be dissipated in the motor to the areas that are relatively easy. This scheme is more useful in the motor which use internal air cooling. Therefore, theoretically, the optimized model can reduce the temperature rise of PMs and the motor.

This section will establish a temperature rise model for the motor, and compare the temperature rise of the original model and the optimized model 2 through simulation based on the comparison with the temperature rise experiment in advance.

A. TEMPERATURE FIELD MODEL OF LHDD-PMSM

The thermal load of LHDD-PMSM consists of several parts: copper loss, core loss of stator and rotor, EDC loss of PMs, and iron loss of slot wedge. These losses are calculated by electromagnetic fields and serve as thermal load for temperature field calculations. Table 10 shows the losses of the original model and the optimized one of LHDD-PMSM under rated load.

TABLE 10. Loss comparison.

	Original	Optimized
Core Loss (W)	8421.2	8502.3
Copper Loss (W)	8652.1	8652.1
EDC Loss of PMs (W)	3476.7	323.5
Iron Loss of Slot Wedge (W)	/	134.8

The values of thermal conductivity λ and specific heat capacity c_ρ of materials in the motor are shown in Table 11.

TABLE 11. Thermal properties of materials.

	λ (W/ (m·°C))	c_ρ (J/(kg·°C))
Air	0.026	1007
Copper	400	385
Laminated Steel(x/y/z)	42.5/42.5/0.57	460
Nd-Fe-B PM	10	370
SMC	20	460
Structure Steel	60.5	434

LHDD-PMSM has two types of convection cooling: one is water cooling through outer water channel, with a convection heat dissipation coefficient of α_1. The second is air gap cooling, with a coefficient of α_2. To improve the simulation efficiency of the solution, calculate the average heat dissipation coefficient as the convective heat dissipation coefficient on the heat exchange surface. The values of α_1 and α_2 are shown in Table 12.

TABLE 12. Convective heat transfer coefficient.

	α_1	α_2
Value (W/m^2·K)	507.05	73.08

The electromagnetic and temperature field of the motor are not isolated [20], [21]. Therefore, the simulation requires a bidirectional coupling between the electromagnetic and temperature fields. Firstly, the initial losses of the motor are calculated using the electromagnetic FEM, and these losses are imported into the temperature field simulation as heat sources. Secondly, the average temperatures of the PMs and windings are obtained from the motor's temperature field FEM, and these temperatures are then fed back into the electromagnetic FEM to adjust the operating points of the PMs on the demagnetization curve and modify the winding's resistance value. This iterative process continues until convergence is achieved, with the convergence criterion being that the maximum difference between the calculated motor temperature rise in consecutive iterations is less than 3%. The bidirectional magneto-thermal coupling simulation process is illustrated in Fig. 25.

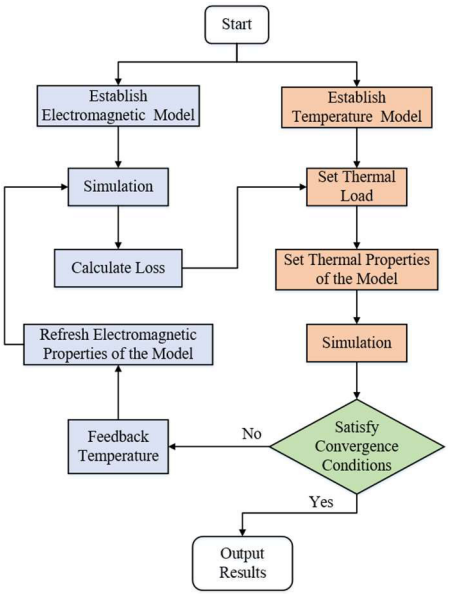

FIGURE 25. Coupled simulation analysis process.

The end structure and the skin effect of the windings are ignored in the model, and it is assumed that all heat acts on the effective part and is uniformly distributed on the cross-section of the winding. As shown in Fig.26, a FEM of the temperature field of the motor is established.

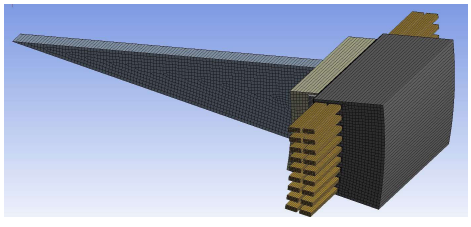

FIGURE 26. FEM model of temperature field of the motor.

B. TEMPERATURE RISE EXPERIMENT

In order to validate the accuracy of the simulation model, continuous load temperature rise experiments are conducted on LHDD-PMSM. Select the data of two temperature sensors in the motor for comparison. Sensor 1 is located at the connection between the stator yoke and the shell, and sensor 2 is located at the connection between the stator teeth and the yoke. Their temperatures can be obtained through the upper computer of the pump station.

Simulations and experiments are then carried out. The comparison and calculation errors of the results are shown in Table 13. Fig.27 shows the temperature rise curve of the experiment and simulation at temperature measuring point 1. From the figure, it can be seen that the coupling model of the motor converges after three iterations.

TABLE 13. Comparison of stable temperatures.

	Experiment	Simulation	Error
Point 1 (°C)	64.5	59.8	7.3%
Point 2 (°C)	41.1	40.1	2.4%

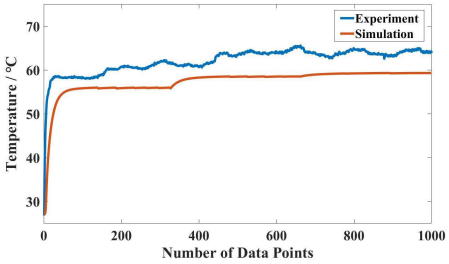

FIGURE 27. Temperature stabilization process of experiment and simulation.

From the data in the table, it can be seen that the error between simulation and experiment can be limited within 10%, indicating that the simulation model established in this section can reflect the temperature distribution of LHDD-PMSM, so it can be used as a tool to compare the temperature rise of different motor design.

C. COMPARISON OF TEMPERATURE RISE BETWEEN ORIGINAL MODEL WITH OPTIMIZED MODEL

Fig.28 shows temperature comparison between the original and the optimized model of LHDD-PMSM in steady-state, and the average temperature of each part of the motor is shown in Table 14.

From the table, it can be seen that after optimizing the EDC loss of the PMs, the average temperature rise in each area of the motor has decreased. Since this paper mainly focuses on the loss optimizing of PMs, the reduction of temperature rise of the rotor is better than that of the stator.

In summary, the results show that by introducing a mixed structure slot wedge and rotor magnetic insulation slot, the EDC loss of the PMs can be significantly reduced,

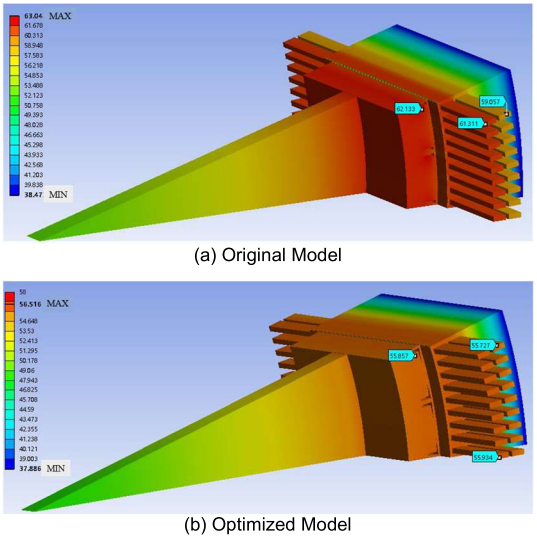

(a) Original Model

(b) Optimized Model

FIGURE 28. Temperature distribution comparison.

TABLE 14. Comparison of a verage temperature.

	Original(°C)	Optimized(°C)	Reduction
Motor	59.01	53.94	8.59%
Winding	60.17	55.81	7.25%
Stator Core	52.31	49.26	5.83%
Rotor Core	61.57	55.82	9.34%
Magnet	61.78	55.86	9.58%
Slot Wedge	/	55.87	/

thereby improving the magneto-thermal stability of the LHDD-PMSM.

VI. CONCLUSION

LHDD-PMSM will continue to heat up during continuous load operation and lead to reversible demagnetization on PMs, which will cause a positive feedback temperature rise in the motor, resulting in higher temperature, higher losses, and lower efficiency.

Online measurement of no-load back EMF of PMSM is an effective method to determine whether the PMs are demagnetized or not. In this paper, a method based on sine wave equivalence for fast measurement of no-load back EMF is proposed. Based on this method, a tester is designed and LHDD-PMSM demagnetization experiments under continuous load are carried out. The experimental results show that after 7 days of continuous operation, the residual magnetic density of the PM decrease by 4.5%, and the magnetic property can be recovered after cooling.

Losses are the fundamental reason of reversible demagnetization of PMs. From the perspective of optimizing tooth harmonics and reducing harmonic distortion, this paper proposes a mixed structure magnetic slot wedge and a rotor magnetic insulation slot, and then proposes an optimized model by combining the slot wedge and rotor insulation slot, which reduces the EDC loss of PMs by 90.7% under rated load. With the introduction of the new structure, the temperature of the rotor core and PMs is reduced by approximately 10% compared to the original, and the lower temperature rise contributes to the magneto-thermal stability of the LHDD-PMSM during continuous load operation.

REFERENCES

[1] K.-Y. Hwang and K.-Y. Yoon, "Fault-tolerant design process of spoke-type IPM motor considering irreversible demagnetization of PM in integrated electric brake system," *IEEE Trans. Magn.*, vol. 58, no. 11, pp. 1–9, Nov. 2022.

[2] F. Yu, L. Yao, S. Chen, Y. Wang, and J.-X. Shen, "Demagnetization analysis and optimization design of interior permanent magnet synchronous motor," in *Proc. 23rd Int. Conf. Electr. Mach. Syst. (ICEMS)*, Hamamatsu, Japan, Nov. 2020, pp. 704–709.

[3] T. A. Huynh and M.-F. Hsieh, "Irreversible demagnetization analysis for multilayer magnets of permanent magnet-assisted synchronous reluctance machines considering current phase angle," *IEEE Trans. Magn.*, vol. 55, no. 7, pp. 1–9, Jul. 2019.

[4] S. T. Lee, "Demagnetization study of an interior permanent magnet synchronous machine considering transient peak 3 phase short circuit current," in *Proc. IEEE Energy Convers. Congr. Expo. (ECCE)*, Cincinnati, OH, USA, Oct. 2017, pp. 4694–4698.

[5] K.-T. Kim, Y.-S. Lee, and J. Hur, "Transient analysis of irreversible demagnetization of permanent-magnet brushless DC motor with interturn fault under the operating state," *IEEE Trans. Ind. Appl.*, vol. 50, no. 5, pp. 3357–3364, Sep. 2014.

[6] P. Zhou, D. Lin, Y. Xiao, N. Lambert, and M. A. Rahman, "Temperature-dependent demagnetization model of permanent magnets for finite element analysis," *IEEE Trans. Magn.*, vol. 48, no. 2, pp. 1031–1034, Feb. 2012.

[7] S. Ruoho, J. Kolehmainen, J. Ikaheimo, and A. Arkkio, "Interdependence of demagnetization, loading, and temperature rise in a permanent-magnet synchronous motor," *IEEE Trans. Magn.*, vol. 46, no. 3, pp. 949–953, Mar. 2010.

[8] P. Zhao and Y. Yu, "Analysis of influence of permanent magnet demagnetization on motor temperature rise," *J. Phys., Conf. Ser.*, vol. 2395, no. 1, Dec. 2022, Art. no. 012022.

[9] J.-X. Shen and X.-F. Qin, "Investigation of rotor eddy current loss in high-speed PM synchronous motor with various PWM strategies," in *Proc. 15th Int. Conf. Ecol. Vehicles Renew. Energies (EVER)*, Monte-Carlo, Monaco, Sep. 2020, pp. 1–5.

[10] H. Fang, D. Li, R. Qu, J. Li, C. Wang, and B. Song, "Rotor design and eddy-current loss suppression for high-speed machines with a solid-PM rotor," *IEEE Trans. Ind. Appl.*, vol. 55, no. 1, pp. 448–457, Jan. 2019.

[11] H. N. Phyu, N. L. H. Aung, and J. Quan, "Investigation of the effect of winding structure and MMF harmonics on the rotor eddy current loss of high speed permanent magnet motor," in *Proc. IEEE Region 10 Conf. (TENCON)*, Singapore, Nov. 2016, pp. 204–209.

[12] P. Zhou, Y. Xu, and X. Xu, "Study on eddy current loss of permanent magnet and performance improvement in low-speed high-torque permanent magnet synchronous motor," in *Proc. IEEE 20th Biennial Conf. Electromagn. Field Comput. (CEFC)*, Denver, CO, USA, Oct. 2022, pp. 1–2.

[13] G. Choi, Y. Zhang, and T. M. Jahns, "Experimental verification of rotor demagnetization in a fractional-slot concentrated-winding PM synchronous machine under drive fault conditions," *IEEE Trans. Ind. Appl.*, vol. 53, no. 4, pp. 3467–3475, Jul. 2017.

[14] Z. Zhang, Z. Deng, Q. Sun, Z. Xu, and K. Li, "Influences of copper shield on eddy-current loss and stress for a rotor of high-speed PM BLDC motor," *Proc. Chin. Soc. Elect. Eng.*, vol. 38, no. 8, pp. 2476–2486, 2018.

[15] J.-R.-R. Ruiz, A. G. Espinosa, L. Romeral, and J. Cusidó, "Demagnetization diagnosis in permanent magnet synchronous motors under non-stationary speed conditions," *Electr. Power Syst. Res.*, vol. 80, no. 10, pp. 1277–1285, Oct. 2010.

[16] C. Wang, M. D. Prieto, L. Romeral, Z. Chen, F. Blaabjerg, and X. Liu, "Detection of partial demagnetization fault in PMSMs operating under nonstationary conditions," *IEEE Trans. Magn.*, vol. 52, no. 7, pp. 1–4, Jul. 2016.

[17] W. Zhang, Y. Xu, and G. Zhou, "Research on a novel transverse flux permanent magnet motor with hybrid stator core and disk-type rotor for industrial robot applications," *IEEE Trans. Ind. Electron.*, vol. 68, no. 11, pp. 11223–11233, Nov. 2021.
[18] W. Zhang, Y. Xu, and M. Sun, "Design of a novel claw pole transverse flux permanent magnet motor based on hybrid stator core," *IEEE Trans. Magn.*, vol. 57, no. 6, pp. 1–5, Jun. 2021.
[19] E. Pošković, F. Franchini, and L. Ferraris, "The magnetization effect on soft magnetic composite prepared stators of axial flux motors," in *Proc. IEEE Energy Convers. Congr. Expo. (ECCE)*, Detroit, MI, USA, Oct. 2022, pp. 1–7.
[20] H. Li, P. T. Krein, and J.-M. Jin, "Electromagnetic-thermal modeling of nonlinear magnetic materials," *IEEE J. Multiscale Multiphys. Comput. Techn.*, vol. 8, pp. 1–10, 2023.
[21] X. Hu, G. Shi, Y. Lai, J. Yu, L. Wang, and Y. Song, "Temperature rise calculation of the high speed magnetic suspension motor based on bidirectional electromagnetic–thermal–fluid coupling analysis," *Machines*, vol. 11, no. 3, p. 364, Mar. 2023.

PENG ZHOU was born in Shandong, China. He received the B.S. degree from the Qingdao University of Science and Technology, Qingdao, China, in 2016, and the M.Sc. degree from Shandong University, Jinan, China, in 2023, where he is currently pursuing the D.Eng. degree in electrical engineering with the School of Electrical Engineering.

His research interests include design and multi-physics analysis of permanent magnet machine and special electrical machines.

YANLIANG XU was born in Shandong, China. He received the B.S. and M.Sc. degrees in electrical machines from the Shandong University of Technology, Shandong, in 1989 and 1994, respectively, and the Ph.D. degree in electrical machines from the Shenyang University of Technology, Shenyang, China, in 2001.

He is currently a Professor with the School of Electrical Engineering, Shandong University. He is also the Head of the Institute of Electrical Machine. His research interests include electrical machines, especially permanent magnet electrical machines and special electrical machines.

FENG XIN was born in Shandong, China. He received the bachelor's degree from the Shandong University of Technology, in 2001.

In 2001, he joined the Shandong Institute for Product Quality Inspection as an Engineer. His current research interests include electrical engineering and electric apparatus and test.